CANCER

Radiogenomic-based multiomic analysis reveals imaging intratumor heterogeneity phenotypes and therapeutic targets

Guan-Hua Su[1]†, Yi Xiao[1]†, Chao You[2]†, Ren-Cheng Zheng[3]†, Shen Zhao[1]†, Shi-Yun Sun[2], Jia-Yin Zhou[2], Lu-Yi Lin[2], He Wang[3]*, Zhi-Ming Shao[1]*, Ya-Jia Gu[2]*, Yi-Zhou Jiang[1]*

Intratumor heterogeneity (ITH) profoundly affects therapeutic responses and clinical outcomes. However, the widespread methods for assessing ITH based on genomic sequencing or pathological slides, which rely on limited tissue samples, may lead to inaccuracies due to potential sampling biases. Using a newly established multicenter breast cancer radio-multiomic dataset (n = 1474) encompassing radiomic features extracted from dynamic contrast–enhanced magnetic resonance images, we formulated a noninvasive radiomics methodology to effectively investigate ITH. Imaging ITH (IITH) was associated with genomic and pathological ITH, predicting poor prognosis independently in breast cancer. Through multiomic analysis, we identified activated oncogenic pathways and metabolic dysregulation in high-IITH tumors. Integrated metabolomic and transcriptomic analyses highlighted ferroptosis as a vulnerability and potential therapeutic target of high-IITH tumors. Collectively, this work emphasizes the superiority of radiomics in capturing ITH. Furthermore, we provide insights into the biological basis of IITH and propose therapeutic targets for breast cancers with elevated IITH.

INTRODUCTION

Breast cancer is the most frequently diagnosed cancer worldwide, becoming a great concern regarding women's health (*1*). Over the past two decades, the intertumoral heterogeneity of breast cancer has been extensively recognized, and precision therapy based on molecular subtypes has improved treatment efficacy and prolonged patient survival (*2*, *3*). However, substantial evidence has been reported on treatment failure and disease relapse originating from intratumor heterogeneity (ITH) (*4*, *5*).

ITH is pervasive across multiple types of cancers (*6*–*8*). Because of the complex and multifactorial nature of ITH, multiscale evaluations were reported to thoroughly characterize ITH, encompassing genetic ITH (GITH), histologic ITH, and phenotypical ITH. GITH, the most well-known aspect, refers to the coexistence of distinct cancer subclones within the identical tumor mass (*6*, *9*, *10*). The identification of ITH in breast cancer depends on multiregional biopsy followed by whole-genome sequencing (*11*, *12*) or is deduced from genomic sequencing from single-region biopsy (*13*, *14*). Multiregional sequencing offers more accurate and detailed information on ITH than single-sample sequencing (*15*). However, the difficulty of sampling sufficient high-quality samples constrains its clinical practicability. Histologic ITH, referring to the variability in tumor cell morphology, is assessed by nuclear size and staining intensity on whole histopathological slides (*16*). Nevertheless, it is inevitable that ITH evaluated on pathological slides remains subject to potential sampling bias because it could only reflect cellular heterogeneity on a single section of the whole tumor. Thus, it is of paramount importance to develop a noninvasive and global method for ITH identification.

Radiomics can be used to extract high-throughput quantitative imaging features that depict gray-level distribution and texture variation patterns (*17*). Some radiomic features correlate with imaging textual heterogeneity and cancer prognosis (*17*, *18*). The superiority of radiomics is the ability to noninvasively characterize ITH from intact tumor regions. In addition, radiogenomic analysis connected mesoscopic radiomic features with microscopic molecular features such as somatic mutation landscapes and gene expression profiles, which confers biological illustration to obscure radiomic features (*19*). Recent studies have reported the predictive power of radiomic features for prognosis-related genomic subclones (*20*); however, an in-depth understanding of imaging ITH (IITH) and its biological foundation remains unclear.

Herein, we established a large breast cancer radiomic cohort based on dynamic contrast–enhanced magnetic resonance imaging (DCE-MRI) in three medical centers [our center (n = 711), the Duke University (DUKE) dataset (n = 641), and The Cancer Genome Atlas (TCGA) dataset (n = 122)]. The radiomic data in our center were also matched with multiomic data. We hypothesize that ITH could be assessed by heterogeneity-related radiomic features and that patient subpopulations with distinct imaging heterogeneity harbor particular biological characteristics. First, we identified and validated IITH phenotypes and their prognostic value through multicenter analysis. Furthermore, we harnessed genomics data and digital pathology to testify the consistency of ITH assessed by radiomic features, genomic alteration patterns, and cellular characteristics. Last, we delved into the biological implications of imaging heterogeneous phenotypes using

[1]Key Laboratory of Breast Cancer in Shanghai, Department of Breast Surgery, Fudan University Shanghai Cancer Center and Department of Oncology, Shanghai Medical College, Fudan University, Shanghai 200032, China. [2]Department of Radiology, Fudan University Shanghai Cancer Center and Department of Oncology, Shanghai Medical College, Fudan University, Shanghai 200032, China. [3]Institute of Science and Technology for Brain-inspired Intelligence, Fudan University, Shanghai 201203, China.
*Corresponding author. Email: yizhoujiang@fudan.edu.cn (Y.-Z.J.); cjr.guyajia@vip.163.com (Y.-J.G.); zhimingshao@fudan.edu.cn (Z.-M.S.); hewang@fudan.edu.cn (H.W.)
†These authors contributed equally to this work.

transcriptomics and metabolomics data, thereby suggesting potential avenues for therapeutic intervention.

RESULTS

Overview of study design and research cohorts

In this study, we sought to develop an IITH phenotype and elucidate its biological significance. To achieve this goal, we divided the study into four phases (Fig. 1). In the first phase, we established three independent radiomic cohorts by curating DCE-MRI images, delineating the tumor region as one of the regions of interest (ROIs) and extracting quantitative radiomic features. In the second phase, we established a radiomic signature to identify IITH subtypes in the discovery and validation cohorts. We also assessed and validated the prognostic power of IITH. In the third phase, we conducted multiscale heterogeneity validation by correlating IITH with

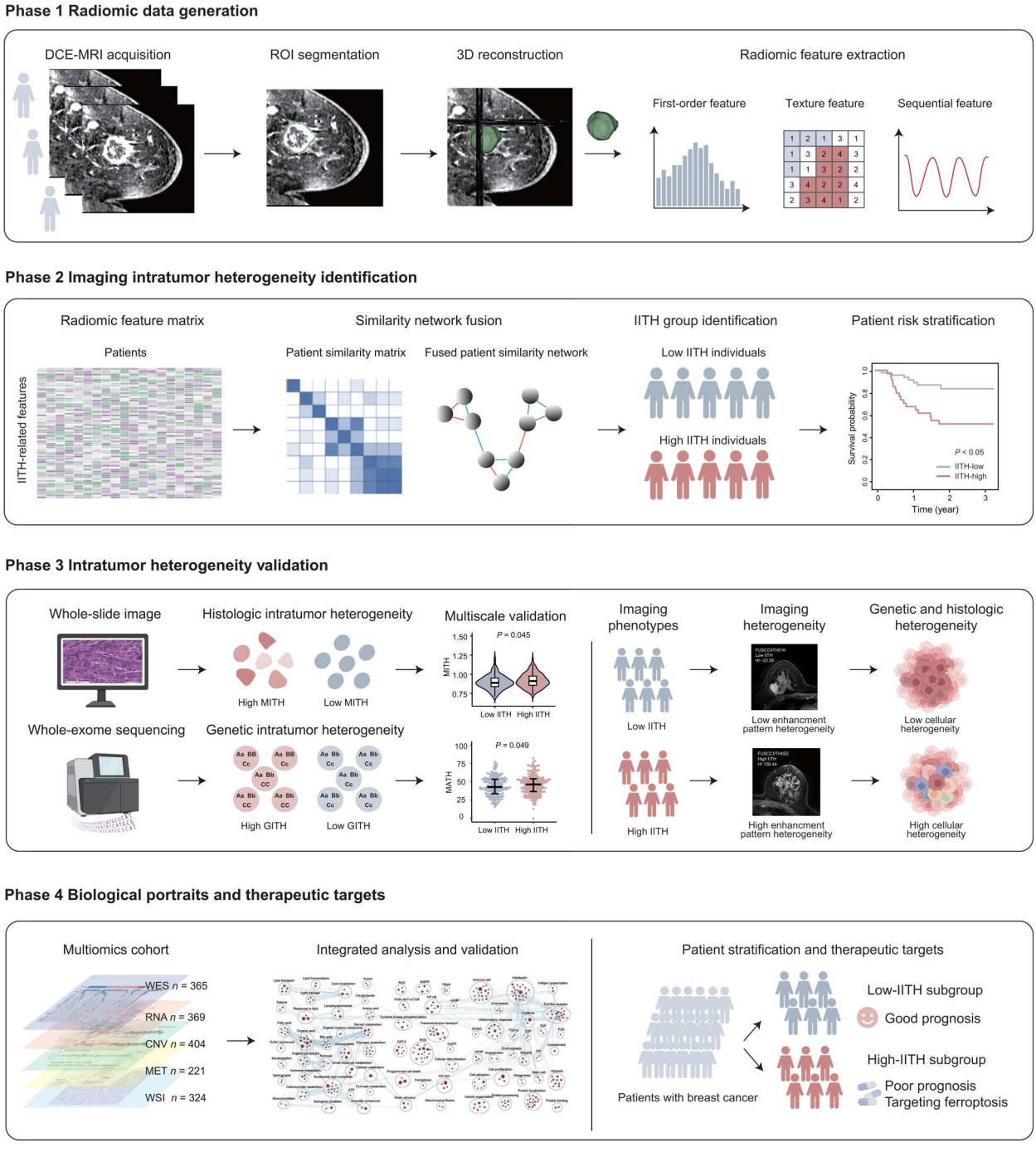

Fig. 1. Schematic of the study. The framework of the four-phase study. IITH, imaging intratumor heterogeneity; MITH, cellular morphological intratumor heterogeneity; GITH, genetic intratumor heterogeneity; WES, whole-exome sequencing; CNV, copy number variation; MET, metabolomics; WSI, whole-slide imaging.

genomic tumor heterogeneity and cellular morphological tumor heterogeneity to verify the robustness of IITH. In the last phase, we explored the molecular portraits and latent therapeutic options for patients with high IITH with a poor prognosis.

We established a large multicenter radiomic dataset (n = 1474) comprising three independent datasets: the Fudan University Shanghai Cancer Center (FUSCC) cohort (cohort 1, n = 711), the DUKE cohort (cohort 2, n = 641), and the TCGA cohort (cohort 3, n = 122). For each radiomic cohort, first-order and texture features were extracted in the precontrast and postcontrast phases from four ROIs. In cohort 1, 468 patients were collected from our multiomic cohort with whole-exome sequencing (n = 365), transcriptomic sequencing (n = 369), copy number variation (n = 404), metabolomics (n = 221), hematoxylin and eosin (H&E)–stained digital pathological images (n = 324), and follow-up (n = 468) data available (fig. S1). Cohort 1 was used to identify imaging heterogeneity and its prognostic significance; validate the correlation among IITH, genomic ITH, and cellular morphological ITH (MITH); and determine the biological hallmarks underlying imaging heterogeneity. In cohort 2, clinical characteristics and follow-up data (n = 618) were available. Cohort 2 was collected to validate the prognostic power of the IITH signature. In cohort 3, matched transcriptomic data (n = 121) were available. Cohort 3 was curated to validate the biological traits of IITH phenotypes (Fig. 2 and Table 1).

Identification of IITH

First, we sought to establish a radiomic signature to evaluate IITH. On the basis of the arithmetic formula and explicit definitions of all extracted radiomic features (*21*), we identified 42 heterogeneity-related first-order and textual radiomic features to assess the IITH of distinct samples (Supplementary Materials, table S1). Considering four ROIs and the different enhanced phases in which the features were extracted, 1968 features were initially included in this analysis. The median absolute deviation (MAD) was calculated to assess the variance in radiomic features among samples, and features with MAD >1 were regarded as highly variable. In the discovery cohort (FUSCC cohort, n = 711), we selected 203 highly variable heterogeneity-related features, including 40 first-order features and 163 textual features (table S2). First-order features and textual features were separately incorporated into similarity network fusion (SNF) to generate two distinct phenotypes (Fig. 3A and fig. S2; see Materials and Methods). Identical criteria and processes were applied to the validation cohorts to identify patients with high and low IITH in the DUKE (n = 641) and TCGA (n = 122) datasets.

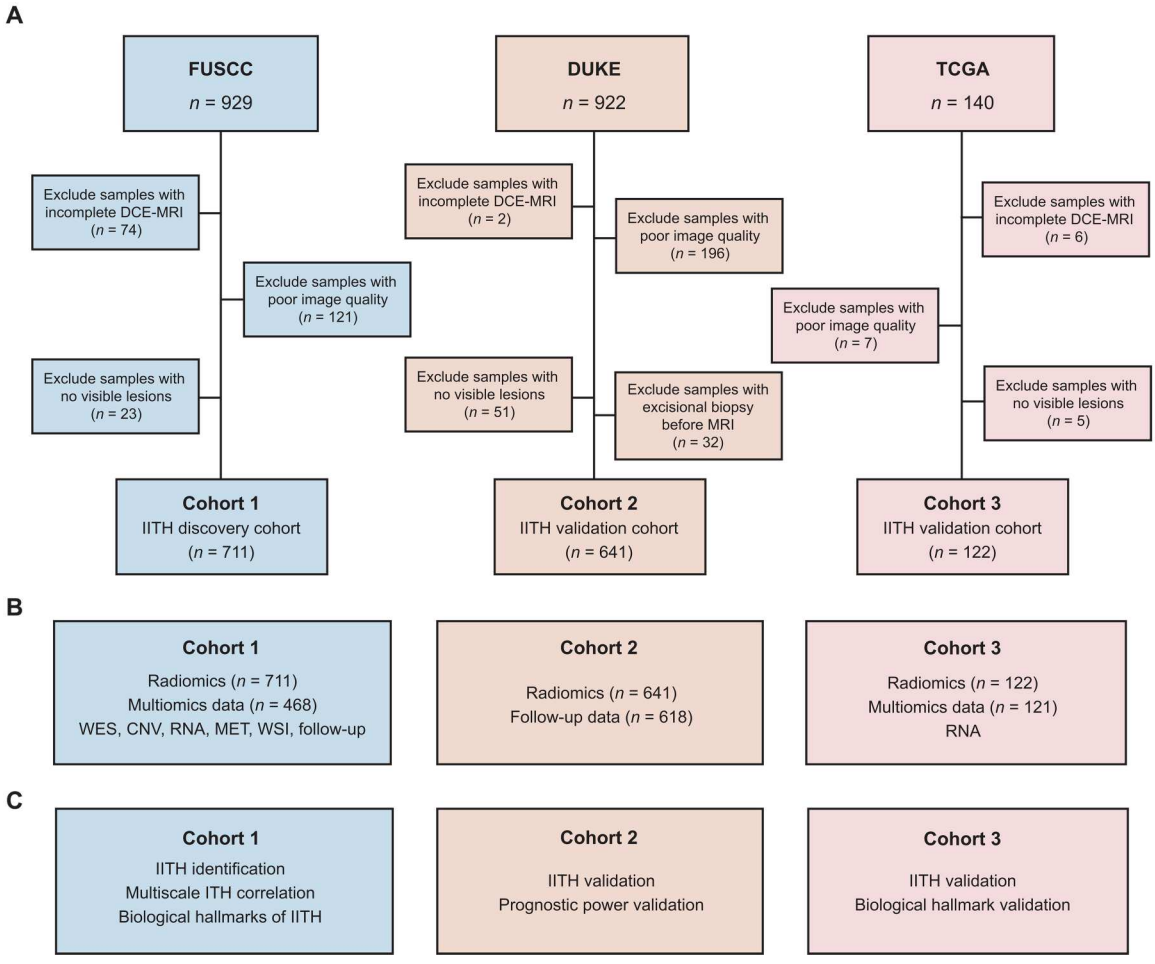

Fig. 2. Cohort overview. (**A**) Flow diagram of the exclusion criteria of the radiomic datasets. (**B**) Sample size of multidimensional data in three datasets. (**C**) The role of the three datasets in this study.

Table 1. Characteristics of patients in the three cohorts. ER, estrogen receptor; PR, progesterone receptor; HER2, human epidermal growth factor receptor 2; NA, not applicable.

		FUSCC (*n* = 711)	DUKE (*n* = 641)	TCGA (*n* = 122)
Age [mean (SD)]		52.6 (10.5)	53.5 (11.4)	53.6 (11.5)
Menopause (%)				
	No	305 (42.9)	265 (41.3)	50 (41.0)
	Yes	396 (55.7)	364 (56.8)	64 (52.5)
	NA	10 (1.4)	12 (1.9)	8 (6.6)
T stage (%)				
	1	304 (42.8)	260 (40.6)	40 (32.8)
	2	382 (53.7)	305 (47.6)	57 (46.7)
	3	18 (2.5)	63 (9.8)	4 (3.3)
	4	0	11 (1.7)	0
	NA	7 (1.0)	2 (0.3)	21 (17.2)
N stage (%)				
	0	361 (50.8)	359 (56.0)	51 (41.8)
	1	188 (26.4)	185 (28.9)	37 (30.3)
	2	91 (12.8)	45 (7.0)	9 (7.4)
	3	65 (9.1)	32 (5.0)	4 (3.3)
	NA	6 (0.8)	20 (3.1)	21 (17.2)
Histology (%)				
	IDC	640 (90.0)	408 (63.7)	97 (79.5)
	ILC	18 (2.5)	43 (6.7)	11 (9.0)
	Others	53 (7.5)	3 (0.5)	3 (2.5)
	NA	0	187 (29.2)	11 (9.0)
Grade (%)				
	1	5 (0.7)	48 (7.5)	27 (22.1)
	2	273 (38.4)	102 (15.9)	67 (54.9)
	3	377 (53.0)	485 (75.7)	17 (13.9)
	NA	56 (7.9)	6 (0.9)	11 (9.0)
ER status (%)				
	Positive	402 (56.5)	481 (75.0)	104 (85.2)
	Negative	309 (43.5)	160 (25.0)	18 (14.8)
PR status (%)				
	Positive	343 (48.2)	418 (65.2)	92 (75.4)
	Negative	367 (51.6)	223 (34.8)	30 (24.6)
	NA	1 (0.1)	0	0
HER2 status (%)				
	Positive	232 (32.6)	112 (17.5)	25 (20.5)
	Negative	479 (67.4)	529 (82.5)	95 (77.9)
	Equivocal	0	0	1 (0.8)
	NA	0	0	1 (0.8)

A comparison of clinicopathological characteristics between the two heterogeneity subtypes is shown in table S3. We found that high-IITH group tumors exhibited higher T stages (cohort 1, P = 0.075; cohort 2, $P < 0.001$; cohort 3, $P = 0.032$) and N stages (cohort 2, $P = 0.004$; cohort 3, $P = 0.035$) and consisted of fewer estrogen receptor (ER)− and progesterone receptor (PR)−positive tumors ($P \leq 0.001$ in cohort 1 and cohort 2). Regarding radiological attributes, high-IITH tumors were larger and more irregular in shape, with a high overall perfusion indicated by the wash-in pattern (fig. S3). Then, we defined the heterogeneity index (HI) as the arithmetic sum of z score normalized features positively related to tumor heterogeneity and the opposite value of features negatively related to tumor heterogeneity. We calculated the HI score of each sample. Correspondingly, a greater HI indicated greater imaging heterogeneity (Fig. 3, B to D).

Representative DCE-MRI images indicated that images with high IITH exhibited a highly heterogeneous enhancement pattern, while low-IITH samples were much more homogeneous (Fig. 3, E and F). Overall, we developed a radiomic signature to identify distinct IITH statuses in large multicenter radiomic cohorts of breast cancer.

Discovery and validation of the prognostic value of IITH

With the long clinical follow-up period of the discovery cohort, we found the prognostic value of IITH. Patients with high IITH presented significantly poorer relapse-free survival (RFS) (log rank P = 0.004; Fig. 3G). A multivariable Cox proportional hazards model showed that high IITH was an independent poor prognostic indicator after adjusting for well-known prognostic factors (tumor size, positive lymph nodes, lymphovascular invasion status, and clinical subtype) {hazard ratio = 2.15 [95% confidence interval (CI): 1.22 to 3.80], P = 0.008; Fig. 3H and Table 2}. Unexpectedly, IITH was also an indicator of overall survival (OS) for patients with breast cancer (log rank P = 0.004; Fig. 3I and Table 2). Furthermore, we externally validated the prognostic power in the DUKE cohort. As described before, we identified patients with high and low IITH in the DUKE dataset, and we found that patients with high IITH had a worse RFS than patients with low IITH (log rank P = 0.003; Fig. 3J). Moreover, multivariable Cox analysis validated the independent prognostic value of IITH in the DUKE cohort [hazard ratio = 1.79 (95% CI: 1.01 to 3.18), P = 0.046; table S4]. In conclusion, we uncovered the independent outcome-predictive power of IITH subtypes.

Correlation of IITH with genomic and pathological ITH

To verify the robustness of IITH, we sought to compare phenotypic IITH with other assessment methods of ITH, such as microscopic genomic heterogeneity and mesoscopic cellular morphological heterogeneity. GITH was measured by the mutant-allele tumor heterogeneity (MATH) algorithm (*22*) (Fig. 4A). An increased MATH value indicates incremental GITH. Patients with high IITH were more genomically heterogeneous than patients with low IITH (P = 0.049; Fig. 4B). In addition, we calculated tumor mutational burden (TMB) and neoantigen load and found that higher TMB (P = 0.005) and neoantigen load (P = 0.043) were present in patients with high IITH (Fig. 4, C and D).

From whole-slide images of H&E-stained tumor slides, we extracted 14 morphological features and 4 texture features characterizing the nuclei of tumor, stromal, and inflammatory cells. We

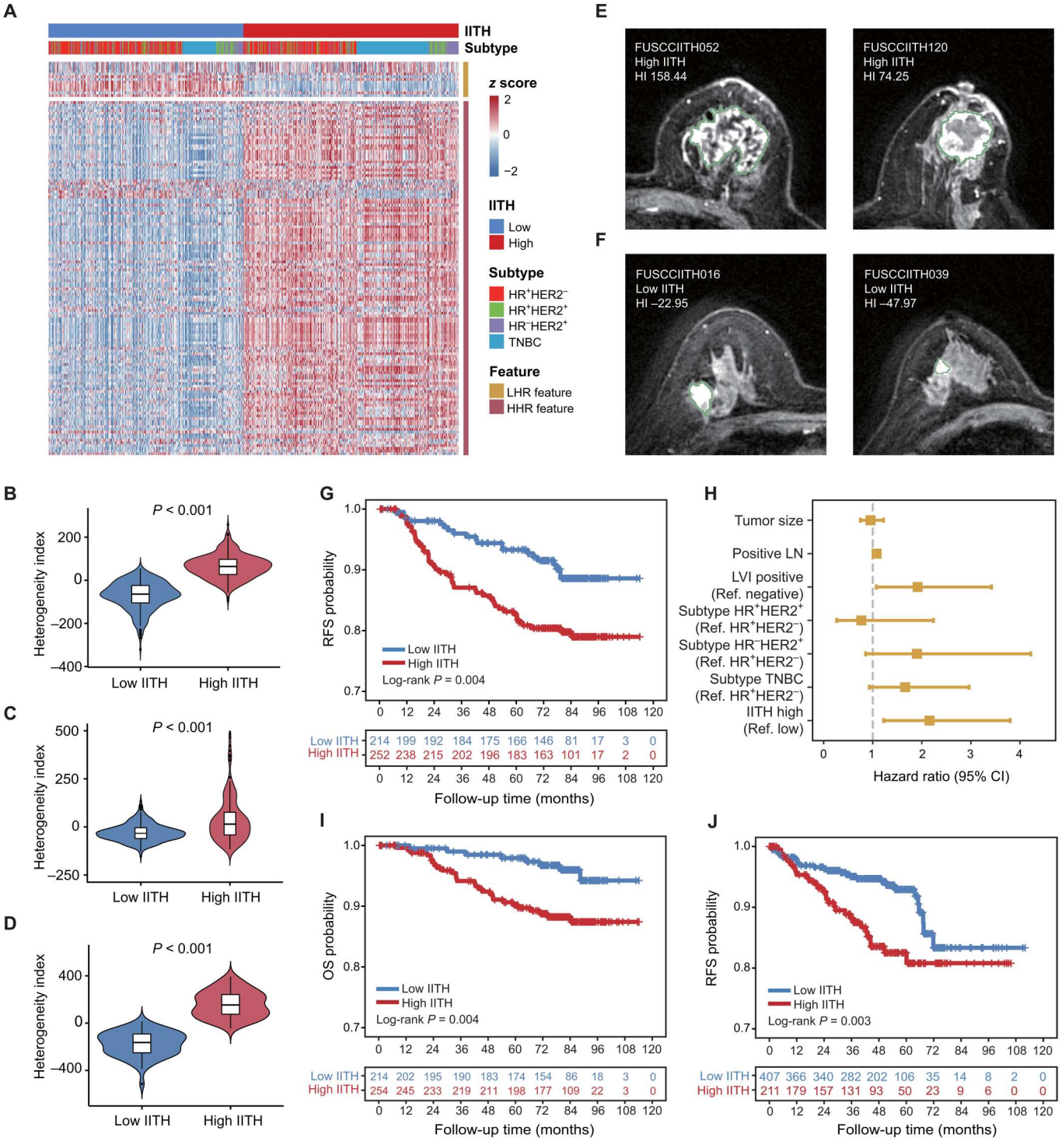

Fig. 3. Identification of IITH phenotypes of breast cancer. (**A**) Heatmap showing unsupervised clustering of heterogeneity-related radiomic features using SNF. Features significantly correlated with the IITH subtype were incorporated. The breast cancer subtypes were also annotated. (**B** to **D**) HI in the FUSCC (B), DUKE (C), and TCGA cohorts (D). HI was calculated for each sample and compared between the high- and low-IITH groups. Comparisons for HI between subgroups were assessed using the Wilcoxon rank-sum test. (**E** and **F**) Representative DCE-MRI images of high (E) and low (F) IITH. Tumor contours were delineated. (**G**) Kaplan-Meier survival curve according to IITH groups for RFS in the FUSCC cohort. (**H**) Forest plot of the multivariable Cox proportional hazards model based on RFS in the FUSCC cohort. (**I**) Kaplan-Meier survival curve according to IITH groups for OS in the FUSCC cohort. (**J**) Kaplan-Meier survival curve according to IITH groups for RFS in the DUKE cohort. LHR, low heterogeneity-related; HHR, high heterogeneity-related; HR, hormone receptor; HER2, human epidermal growth factor receptor 2; TNBC, triple-negative breast cancer; LN, lymph node; LVI, lymphovascular invasion.

Table 2. Multivariate Cox proportional hazard models for RFS and OS in the FUSCC cohort. LN, lymph node; LVI, lymphovascular invasion; HR, hormone receptor; TNBC, triple-negative breast cancer.

Variables		RFS		OS	
		Hazard ratio (95% CI)	*P*	Hazard ratio (95% CI)	*P*
Tumor size	–	0.95 (0.75–1.22)	0.71	1.01 (0.74–1.38)	0.93
Positive LN	–	1.08 (1.05–1.10)	<0.001	1.10 (1.06–1.14)	<0.001
LVI	Negative	Ref			
	Positive	1.91 (1.07–3.42)	0.03	0.88 (0.38–2.04)	0.77
Clinical subtype	HR^+HER2^-	Ref			
	HR^+HER2^+	0.77 (0.26–2.24)	0.63	1.36 (0.28–6.57)	0.70
	HR^-HER2^+	1.90 (0.86–4.22)	0.11	5.21 (1.81–15.05)	0.002
	TNBC	1.66 (0.93–2.96)	0.09	2.08 (0.82–5.26)	0.12
IITH	Low	Ref			
	High	2.15 (1.22–3.80)	0.008	3.02 (1.24–7.33)	0.01

assessed MITH by quantifying the variation in nuclear morphology within each tumor sample. Notably, high-IITH tumors demonstrated elevated MITH in features such as CurvMean (P = 0.009), CurvStd (P = 0.020), and IntensityMax (P = 0.036; Fig. 4, E to G, and fig. S4). In addition, we observed heightened MITH in stromal and inflammatory nuclei (fig. S4). Representative pathological images illustrated cellular ITH, as depicted in Fig. 4 (H and I). In summary, DCE-MRI–derived IITH was consistent with genomic and pathological ITH evaluation.

Genomic, transcriptomic, and metabolomic alterations related to IITH

To investigate the biological basis of the prognostic disparity between high- and low-IITH tumors, we performed multiomic analysis to uncover their molecular distinction. We did not observe many significantly differential high-frequency somatic mutations or copy number variations between high- and low-IITH tumors (fig. S5). In addition, despite higher chromosomal instability (represented by elevated TMB and neoantigen load), effective antitumor immune responses were not elicited in high-IITH tumors (fig. S6). Then, we used gene set enrichment analysis (GSEA) to explore the enriched pathways in high IITH (tables S5 and S6). Oncogenic or cancer hallmark pathways, including Hippo [normalized enrichment score (NES) = 1.86, P = 0.004], RAS (NES = 1.69, P = 0.02), phosphatidylinositol 3-kinase (PI3K)–AKT–mammalian target of rapamycin (mTOR) (NES = 1.53, P = 0.04), and mitogen-activated protein kinase (MAPK) (NES = 1.50, P = 0.05), were up-regulated in high-IITH tumors. Meanwhile, classic malignant behaviors of cancer cells, such as cell proliferation, cell adhesion (NES = 1.60, P = 0.027), protein processing (NES = 1.92, P = 0.002), stem cells (NES = 1.64, P = 0.018), hypoxia (NES = 1.68, P = 0.045), and angiogenesis (NES = 1.59, P = 0.053), were also enriched in high-IITH samples. In particular, high-IITH tumors exhibited a widely dysregulated metabolism comprising up-regulation of fatty acids, amino acids, organic acids, nucleosides, and glycogen (Fig. 5A).

We ranked all the enriched pathways by NES and obtained the most enriched biological processes in the high- and low-IITH groups. We observed that ferroptosis (NES = 2.27, P < 0.001), nuclear factor erythroid 2–related factor 2 (NRF2) (NES = 2.08, P < 0.001), reactive oxygen species (ROS) (NES = 2.00, P < 0.001), and bile acid metabolism (NES = 2.08, P < 0.001) were the most up-regulated pathways in high-IITH tumors, while processes correlated with DNA double-strand breaks (NES = −1.71, P = 0.024) were most activated in low-IITH tumors (Fig. 5B). These results revealed divergent biological characteristics of the two patient subgroups, wherein high-IITH tumors were metabolically exuberant and were confronted with oxidative stress and low-IITH tumors lacked explicit characteristics, with DNA damage repair more common in this population.

On the basis of the enriched metabolic pathways revealed from the transcriptomic analysis, we used differential abundance (DA) score analysis with the metabolomic data of the high- and low-IITH groups. We identified 14 up-regulated pathways among metabolic pathways with more than three annotated metabolites. Among these up-regulated pathways, three were up-regulated with DA scores of at least 0.25 (Fig. 5C). Specifically, multiple metabolic pathways, particularly fatty acid biosynthesis and elongation, were up-regulated in high-IITH tumors (Fig. 5C). Collectively, transcriptomic and metabolomic analyses elucidated that tumors with high imaging heterogeneity were a phenotype of cancer with substantial malignancy and dysregulated metabolism, which endowed these tumor cells with a marked tendency toward ferroptosis.

Ferroptosis is a biological hallmark and potential therapeutic target for high-IITH tumors

We further investigated the most prominent molecular process identified in the transcriptomic analysis. Among the enriched pathways in high-IITH tumors, ferroptosis ranked first (NES = 2.27, P < 0.001, false discovery rate = 0.024; Fig. 6A). We thus generated a ferroptosis pathway score with single-sample GSEA in the discovery and TCGA validation cohorts and confirmed that ferroptosis was significantly up-regulated in high-IITH tumors (Fig. 6, B and C). Consistently, crucial factors of ferroptosis, such as ROS, iron metabolism, and lipid anabolism, were extensively enriched in high-IITH tumors (Fig. 5A).

To validate the hypothesis of a notable up-regulation of ferroptosis in high-IITH tumors, we conducted an integrated multiomic analysis. Initially, we juxtaposed the abundance of lipids and oxidized lipids between high- and low-IITH samples. Comprehensive metabolomic and lipidomic analyses unveiled heightened levels of fatty acids, phosphatidylethanolamine, and oxidized lipids essential for triggering ferroptosis (Fig. 6D). Furthermore, the expression

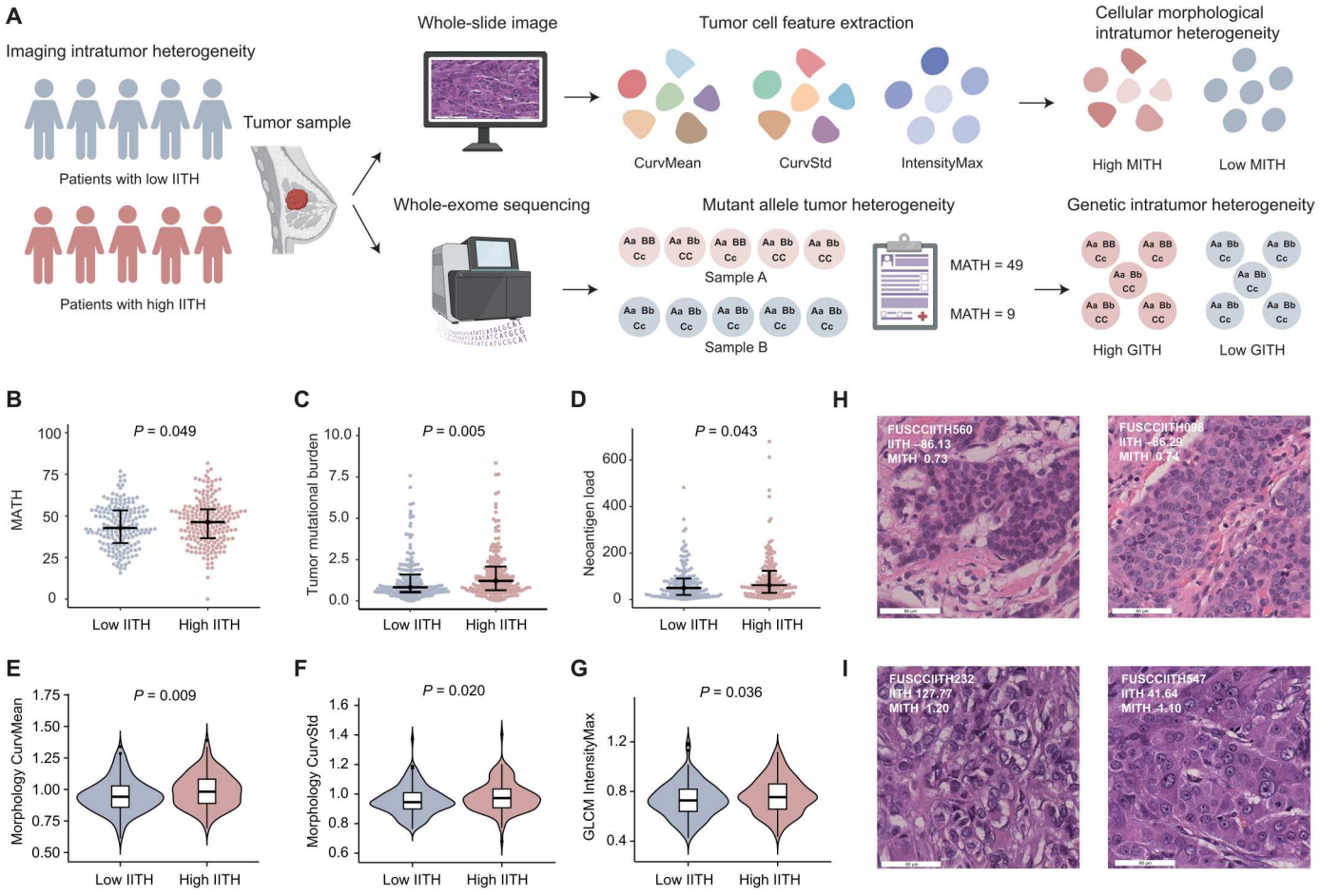

Fig. 4. The correlation between IITH, genomic ITH, and MITH. (**A**) Diagram indicating how histologic ITH and GITH were calculated and used to assess ITH. (**B**) MATH scores across the high- and low-IITH clusters. One-sided Student's *t* test *P* value is shown. (**C** and **D**) Significantly different TMB (C) and neoantigen load (D) in the high- versus low-IITH groups. The *P* values from the Wilcoxon test are shown. (**E** to **G**) MITH scores of representative features CurvMean (E), CurvStd (F), and IntensityMax (G) extracted from tumor cells across high- and low-IITH groups. The *P* values from the Wilcoxon test are shown. (**H** and **I**) Representative pathological images of tumor samples with low (H) and high (I) IITH.

profiles of biological processes crucial for provoking ferroptosis, including iron intake ($P = 0.018$) and utilization ($P = 0.017$), unsaturated fatty acid biosynthesis ($P = 0.078$), and ROS pathways ($P = 0.008$), were elevated in high-IITH samples (Fig. 6E), while pathways suppressing ferroptosis, such as the thioredoxin process, were also augmented ($P = 0.010$; fig. S7). These findings implied that while ferroptosis initiation was pronounced in tumors with high imaging heterogeneity, cancer cells concurrently engaged compensatory mechanisms to hinder programmed cell death as a self-protective strategy. Consequently, by obstructing these inhibitory processes, such as the thioredoxin pathway, we could induce ferroptosis in high-IITH tumors.

We outlined the fundamental pathways of ferroptosis and contrasted the alterations in metabolic gene expression relative to normal tissue between high- and low-IITH tumors (Fig. 6F). As depicted in the figure, high-IITH tumors exhibited activation of the unsaturated fatty acid synthesis, iron transport, Fenton reaction, and thioredoxin pathways (Fig. 6F). We further interrogated radiomic features correlated with tumor ferroptosis (as shown in fig. S8A). Among these, gray-level co-occurrence matrix feature *Difference Entropy* and first-order feature *Variance*, indicative of imaging heterogeneity, emerged as particularly significant (fig. S8, B and C). In summary, we solidified the link between ferroptosis activity and IITH through integrated analysis and proposed potential therapeutic targets for these patients with a poor prognosis.

DISCUSSION

ITH is a crucial factor for treatment resistance and poor clinical outcome. Here, we established a noninvasive DCE-MRI radiomics method to evaluate ITH, which we named IITH. Furthermore, we demonstrated the prognostic power of IITH and its correlation with well-known GITH and MITH. Notably, we systematically uncovered the biological basis and identified ferroptosis as a treatment target for patients with high-IITH breast cancer with a poor prognosis.

In this study, we determined tumor heterogeneity-related radiomic features based on the explicit definition of each PyRadiomic feature. In the first step, we established a set of heterogeneity-related radiomic features. For instance, first-order histogram

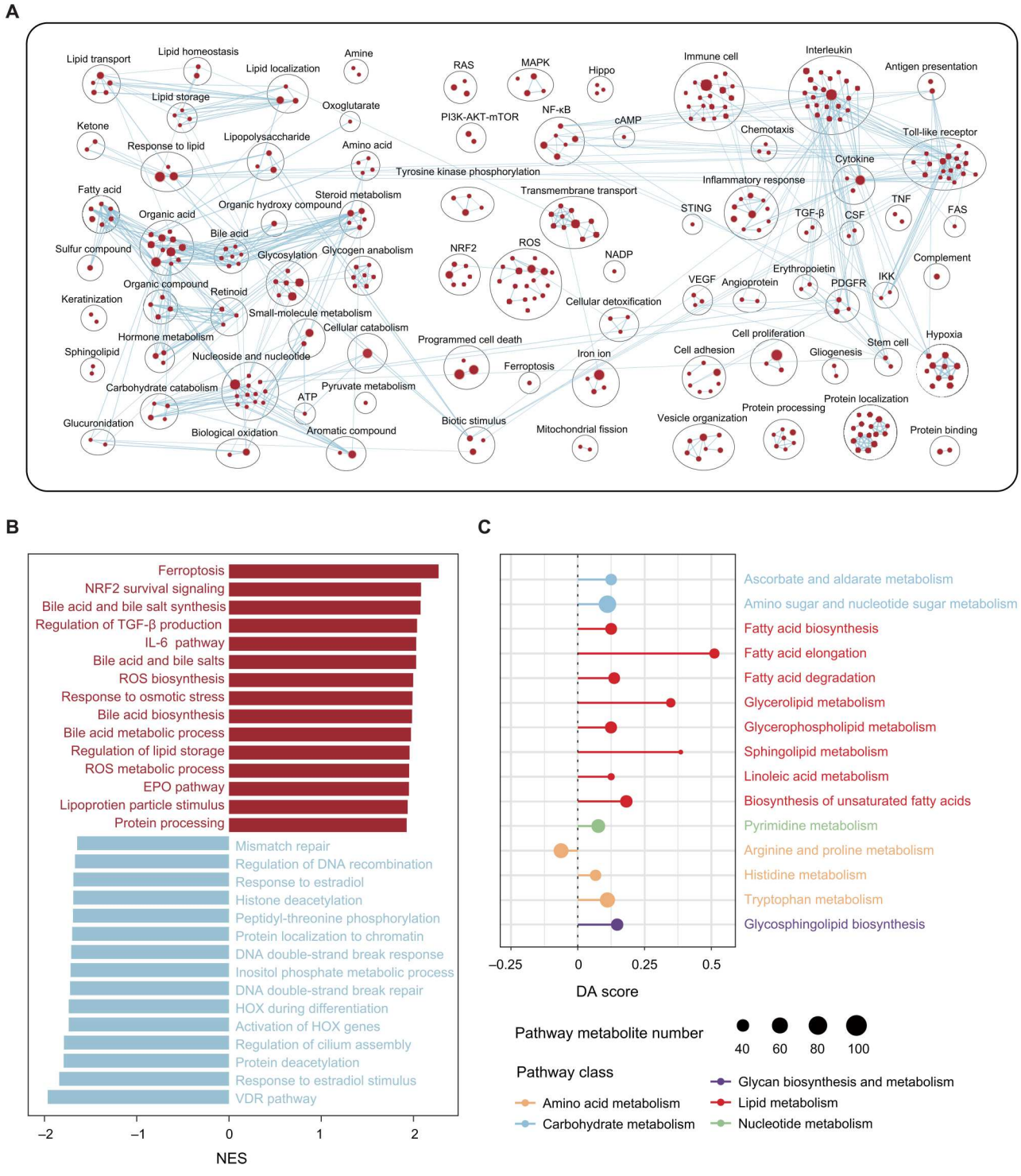

Fig. 5. Biological portraits of high-imaging-heterogeneity breast cancers. (**A**) Network of substantially enriched gene circuits within high-IITH samples from the FUSCC dataset. Nodes represent pathways, and edges represent shared genes between pathways. Network maps were generated for nodes with $P < 0.05$, and nodes sharing gene overlaps with an overlap coefficient > 0.3 were connected by a blue line (edge). (**B**) Bar plot showing the top enriched pathways ordered by the NES in the high-IITH group (red) and low-IITH group (blue) in the FUSCC dataset. (**C**) A pathway-based analysis of metabolomic alterations between IITH groups. The DA score captured the overall change in a metabolic pathway. A score of 1 indicated that all metabolites in this pathway increased in the high-IITH group compared with the low-IITH group, and a score of −1 indicated that all metabolites in this pathway decreased.

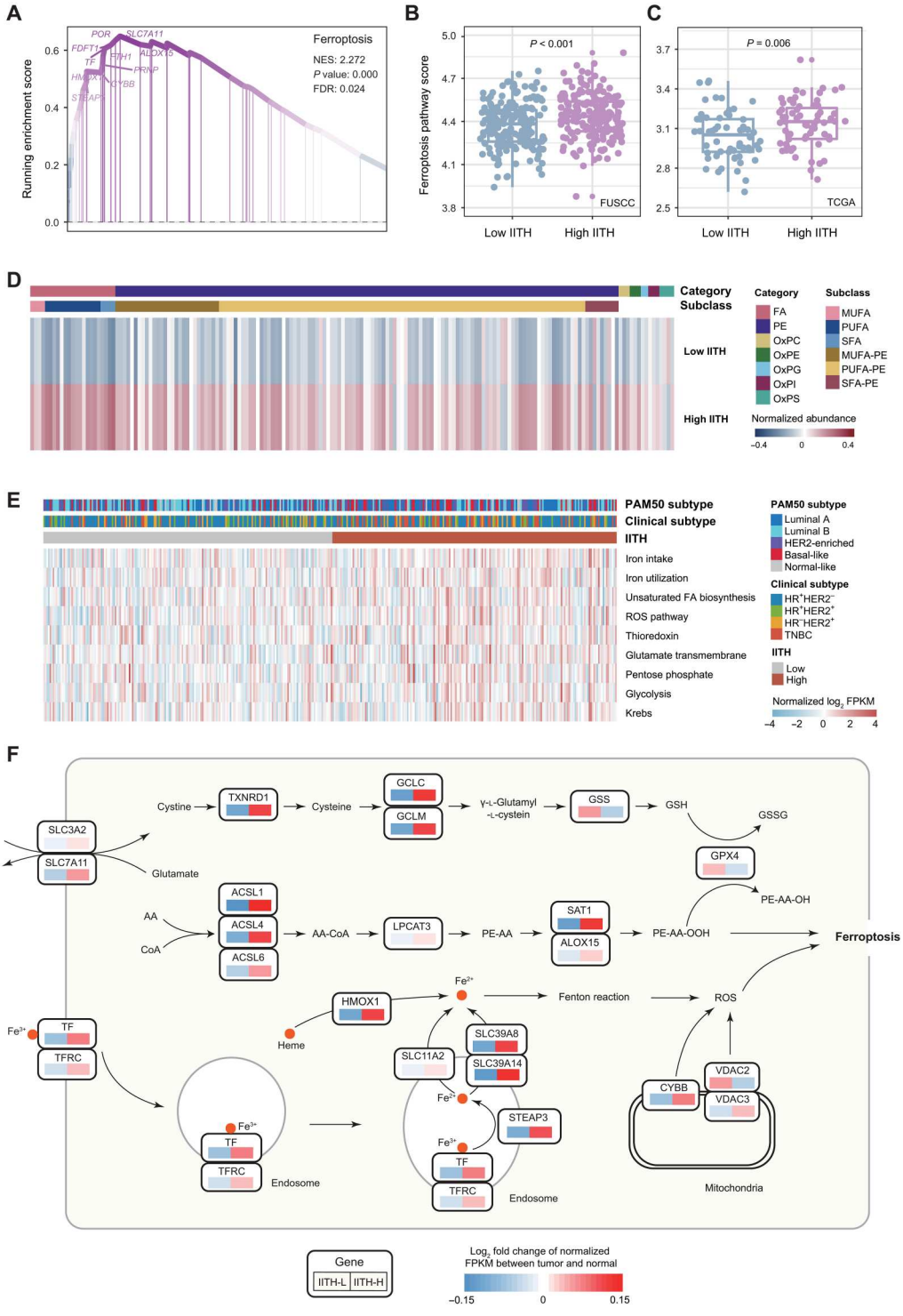

Fig. 6. Ferroptosis is a therapeutic vulnerability of high-imaging-heterogeneity patients. (**A**) The enrichment score of the top enriched pathway, ferroptosis, in high-IITH tumors from GSEA. (**B** and **C**) Distinction of ferroptosis pathway scores across patients with high and low IITH from the FUSCC cohort (B) and TCGA cohort (C). The *P* value from the Wilcoxon test is shown. (**D**) Heatmap depicting the mean normalized abundance of lipids and oxidized lipids detected in high- and low-IITH samples. (**E**) Heatmap of the normalized single-sample GSEA enrichment score of ferroptosis-related pathways. (**F**) Diagram summarizing metabolic genes involved in the essential process of ferroptosis. Relative expression alteration scores were compared between high- and low-IITH samples. The alteration score of each gene was defined as the $\log_2$-fold change in the average normalized mRNA expression in high- and low-IITH samples versus the paired normal tissue. FA, fatty acid; PE, phosphatidylethanolamine; OxPC, oxidized phosphatidylcholine; OxPE, oxidized phosphatidylethanolamine; OxPG, oxidized phosphatidylglycerol; OxPI, oxidized phosphatidylinositol; OxPS, oxidized phosphatidylserine; MUFA, monounsaturated fatty acid; PUFA, polyunsaturated fatty acids; SFA, saturated fatty acid; AA, arachidonic acid; GSH, reduced glutathione; GSSG, oxidized glutathione; IITH-L, low-IITH samples; IITH-H, high-IITH samples; FDR, false discovery rate; FPKM, fragments per kilobase of transcript per million mapped reads.

features depict the number of pixels within a whole image with the same intensity for each intensity level (*23*). The first-order feature *Range* measures the range of gray values in the ROI. It was determined to be positively related to heterogeneity, as a higher value of *Range* reflects higher heterogeneity from the aspect of pixel intensity distribution. Texture analysis takes the spatial information of voxels into consideration and identifies similar patterns in an image and groups them (*23*). *Gray Level Non-Uniformity* measures the variability in gray-level intensity values in the image. It was considered positively related to heterogeneity, as a higher value indicated more heterogeneity in intensity values. After curating the whole set of heterogeneity-related features, we selected features with high intersample variability to cluster samples into high- and low-heterogeneity groups (*24*). It was demonstrated that patients with

high IITH exhibited a significantly poor clinical outcome, regardless of RFS or OS. The consistency with previous studies and external validation in the DUKE DCE-MRI dataset supported the utility of imaging heterogeneity in reflecting cancer prognosis (*25*, *26*). Divergent from the holistic view of imaging heterogeneity provided in the present study, a previous work focused on habitat imaging features extracted from the spatial interaction of subregions with poor, moderate, and marked perfusion, yielding a detailed perspective for spatial heterogeneity measurement (*27*). In future investigations, one may combine the empirical textural features and habitat features to gain a more comprehensive outlook on ITH.

To prove the universality and broaden the application scope of IITH, we conducted multiscale ITH validation and established the connection among IITH, GITH, and MITH (*16*, *22*). Integrated analysis demonstrated that samples with elevated IITH also exhibited higher genomic heterogeneity and higher morphological heterogeneity. As is widely acknowledged, two major disadvantages exist regarding these classical ITH assessment methods. First, GITH and MITH warrant single- or multiregional biopsy followed by whole-exome sequencing and H&E-stained pathological sections followed by computational analysis, respectively (*16*). Their invasive nature limits their clinical application. Second, ITH evaluation is performed on limited regions and layers and lacks an overall assessment of the whole tumor (*28*). The radiomics method overcomes these shortcomings and thoroughly estimates ITH noninvasively (*17*). In addition to GITH, we found that high-IITH tumors harbored an increased TMB and neoantigen load, which shows that heterogeneous tumors on imaging presented genomic instability and generated more somatic mutations and mutation-derived tumor antigens.

We next sought to explore the biological significance underlying the formation of IITH. Phenotypical patterns indicated that high-IITH tumors were large and grotesque, with high perfusion of contrast agent, presumably revealing that these malignant tumors contained more complex tumor vessels and thus showed higher overall early contrast agent perfusion. Radiogenomic analysis revealed molecular pathways characterizing active tumor growth enriched in high-IITH samples but not in low-IITH samples. They comprised cell proliferation, cell adhesion, protein processing, stem cells, hypoxia, and angiogenesis. Consistently, classic cancer hallmark pathways, including RAS, MAPK, PI3K-AKT-mTOR, and Hippo, were up-regulated in high-IITH tumors. It is not hard to speculate that tumors with more heterogeneous enhancement patterns exhibit more malignant biological behaviors than their homogeneous counterparts, resulting in a worse prognosis (*8*, *29*, *30*). Higher pathological T and N stages confirmed their malignant nature as well. In addition, transcriptomic and metabolomic analyses revealed that tumors with high IITH present metabolic activation, particularly lipid and amino acid metabolism, which could be at least partially because these vigorous tumors advance the energy metabolism process to meet their requirement for nutrients (*26*).

Intriguingly, we found significantly activated ferroptosis in tumors with high imaging heterogeneity through integrated multiomic analysis. Ferroptosis is a modality of regulated cell death driven by iron-dependent lipid peroxidation (*31*). It is governed by multiple metabolic pathways involving iron overload, mitochondrial activity, redox systems, and nutrient metabolism (*31*). Recent studies on ferroptosis and MRI have mainly focused on nanoprobes inducing ferroptosis in tumor cells and in vivo tracer imaging (*32*–*34*), while our study is the first to show that ferroptosis can be captured by radiomic signatures through imaging heterogeneity. Here, we hypothesize that tumors with high heterogeneity up-regulate numerous metabolic pathways and are therefore more vulnerable to ferroptosis. The final effect of ferroptosis, the switching of cellular morphology and rupture of the cellular membrane, eventually forms the phenotype of imaging heterogeneity that is captured by quantitative radiomic features. This finding is consistent with the results of previous studies showing that apoptosis-induced therapy could be detected by diffusion-weighted MRI in a preclinical model (*35*). Furthermore, we found that TMB and neoantigens were increased and that the ROS pathway was enriched in patients with high IITH. On the basis of a review article (*7*), we speculated that ROS are internal mutagens that activate oncogenes, yield high TMB, and facilitate ITH. A recently published study reported a positive correlation between ROS and ITH in breast cancer (*36*). Consequently, we propose that ROS are the crucial cross-link between ITH and ferroptosis. In recent decades, studies have elucidated the therapeutic value of targeting ferroptosis in cancers (*37*). Major treatment options comprise promoting ferroptosis and inhibiting suppressor pathways (*38*). In this study, we found that the thioredoxin pathway was a crucial mechanism by which high-IITH tumors might escape ferroptosis. Collectively, ferroptosis inducers targeting thioredoxin, such as ferroptocide, are promising future treatment options for patients with high-IITH breast cancer with a poor prognosis (*39*). However, owing to the nature of identifying ITH but not directly predicting the ferroptosis level, overlap of the ferroptosis score did exist between the high- and low-IITH subtypes although the difference was statistically significant. This limitation drove us to identify radiomic features significantly associated with ferroptosis. *Variance* and *Difference Entropy* measure the statistical dispersion gray-level intensity within an ROI and the average difference and irregularity in gray-level intensity between neighboring pixels or voxels, respectively. This provided a clue that complex or heterogeneous image texture and ferroptosis were interconnected, which substantiated the association between ferroptosis and imaging heterogeneity from another perspective and established a direct relationship between microscopic and phenotypic alterations.

Our study has several limitations. First, our study is a retrospective cohort study. Although we validated the evaluation of IITH and its prognostic value in the DUKE dataset with a large sample size, the clinical utility of IITH warrants prospective validation. Second, limited by the technical bottleneck and analytic nature of the study design, there is a lack of experimental evidence of the biological significance of imaging heterogeneity. Thus, we conducted a large-cohort multiomic analysis and performed external validation in the TCGA cohort to test our results from multiple dimensions. Third, albeit widely used, conventional textual features might be sensitive to variations in imaging protocols and acquisition parameters. Robust handcrafted features for radiomic analysis provided a paradigm for future studies (*40*).

In summary, in this multicenter radio-multiomics cohort study, we identified the distinct phenotypes of ITH assessed by DCE-MRI radiomic features and their prognostic value. Furthermore, with genomic, transcriptomic, metabolomic, and digital pathological data, we comprehensively validated this heterogeneity assessment method from mesoscopic to microscopic scales and revealed the biological behavior in tumors with high IITH. Notably, we reported

ferroptosis as a vulnerability of breast cancers with high IITH and as a promising target in the era of precision oncology.

MATERIALS AND METHODS

The cohort

A total of 1991 patients from three independent datasets were incorporated in this study for (i) imaging heterogeneity identification and prognostic power assessment; (ii) radio-multiomic analysis of the association among imaging heterogeneity, genomic heterogeneity, and cellular morphological heterogeneity; and (iii) radio-multiomic analysis of the biological basis of imaging heterogeneity (Fig. 1). The clinical characteristics of these cohorts are shown in Table 1.

Cohort 1 (FUSCC dataset) comprised 929 patients with primary breast cancer treated at FUSCC between August 2009 and May 2015. The exclusion criteria included incomplete DCE-MRI (n = 74), poor image quality (n = 121), and no visible lesions that could be accurately identified and mapped by radiologists (n = 23). A total of 711 samples were retained in this cohort. In this radiomic cohort, 468 patients were curated from our multiomic cohort with whole-exome sequencing (n = 365), transcriptomic sequencing (n = 369), copy number variation (n = 404), metabolomics (n = 221), H&E-stained digital pathological section (n = 324), and follow-up (n = 468) data available (fig. S1). In this patient cohort, follow-up was completed on 30 June 2021, and the median length of follow-up was 83.4 months. RFS was defined as the time from diagnosis to the first recurrence, a diagnosis of contralateral breast cancer or death from any cause. OS was defined as the time from the date of surgery to death from any cause. Patients without events were censored at the time of the last follow-up. The independent ethics committee/institutional review board of FUSCC approved the study, and the requirement for written informed consent was waived for this retrospective study.

Cohort 2 (DUKE dataset) contained 922 patients with breast cancer with matched radiomics and follow-up data from The Cancer Imaging Archive (TCIA)–DUKE dataset. The exclusion criteria were incomplete DCE-MRI (n = 2), excisional biopsy before MRI (n = 32), poor image quality (n = 196), and no visible lesions (n = 51). A total of 641 samples were retained in this cohort, among which 618 samples had intact follow-up data.

Cohort 3 (TCGA dataset) consisted of 140 patients with breast cancer with matched radiomic and transcriptomic sequencing data from the TCIA-TCGA dataset. The exclusion criteria were incomplete DCE-MRI (n = 6), poor image quality (n = 7), and no visible lesions (n = 5). Last, 122 samples were retained in this cohort, among which 121 samples had transcriptomic data. Data from cohort 2 and cohort 3 are publicly available on the TCIA, and informed consent was waived. The use of these data does not require approval from an ethics committee or institutional review board as there is no identifiable patient information involved (*41*).

Cohort 1 was collected to identify imaging heterogeneity and prognostic significance; validate the correlation among IITH, genomic heterogeneity, and cellular heterogeneity; and determine the biological hallmarks of imaging heterogeneity. Cohorts 2 and 3 were curated to validate the prognostic power and biological traits of IITH, respectively.

Heterogeneity-related radiomic features

Next, we selected radiomic features most correlated with imaging heterogeneity as imaging heterogeneity-related features according to the definition of the PyRadiomics package (https://pyradiomics.readthedocs.io/en/latest/features.html). For first-order features, we selected features characterizing the variation in intensity values, and for textural features, we selected features depicting heterogeneous or homogeneous textural patterns. Last, 42 radiomic features (9 first-order features and 33 texture features) were identified as heterogeneity-related features. The definition of each heterogeneity-related feature is described in the Supplementary Materials and table S1. Considering four ROIs and the different enhanced phases in which the features were extracted, 1968 features were initially contained in the clustering analysis.

Imaging heterogeneity phenotypes

We performed SNF [using the R package "SNFtool" (*42*)] to identify distinct imaging heterogeneity phenotypes, considering that first-order and textural features were quite different and could be regarded as different data dimensions. MAD was used to assess the variability of heterogeneity-related radiomic features where MAD >1 was defined as high intersample variability. MAD is a measure of the variability of univariate quantitative data similar to the SD but more robust to outliers (*43*). The top 203 variable features (40 first-order and 163 textual features) were used in this clustering analysis (table S2). We then computed the squared Euclidean distances for normalized first-order and textual feature matrices using the function "dist2" in the R package "SNFtools." According to the pairwise squared Euclidean distance matrices, a similarity network was constructed by the functions "affinityMatrix" and "SNF" in the R package SNFtools. All the parameters were set as follows: K = 13, sigma = 0.4, and t = 20. Two was identified as the optimal number of clusters for the similarity network using the function "Spectrum" in the R package Spectrum. Last, we conducted spectral clustering by the function "spectralClustering" (R package SNFtools). Given the definition of each candidate radiomic feature, most of them were positively correlated with image heterogeneity (high ITH related), and the remaining features were negatively correlated with image heterogeneity (low ITH related). An HI was then calculated for each individual, defined as the arithmetic sum of z score normalized positive features and the opposite value of negative features, whereby a higher HI represents higher IITH and vice versa.

Extrapolation of the imaging heterogeneity subtype was conducted in the DUKE and TCGA cohorts following the same procedure as the FUSCC cohort. Variable radiomic features were selected through the criterion of MAD >1 and the SNF parameter was the same as that used in the FUSCC cohort. HI was calculated in these two cohorts to distinguish high- and low-IITH subpopulations.

Multiomics data generation and analysis

Sample processing for genomic DNA and total RNA extraction, multiomic sequencing procedures, and bioinformatic operations and analyses including whole-exome sequencing, copy number alterations, RNA sequencing, metabolomics, and lipidomics are presented in the Supplementary Materials.

Statistical analysis

Student's *t* test and Wilcoxon test were used to compare continuous variables between groups. Pearson and Spearman tests were used to evaluate the correlation of continuous variables. Before the comparisons, the normality of the distributions was tested with the Shapiro-Wilk test. Pearson's chi-square test, and Fisher's exact test were used for the comparison of unordered categorical variables. To explore the association between imaging phenotypes and survival, Kaplan-Meier analysis and the Cox proportional hazards model were used. Differences in survival between groups were evaluated by the log rank test. In general, tests were two sided, and $P < 0.05$ was regarded as statistically significant unless otherwise specified. All statistical analyses were performed using R software (version 4.1.1).

Supplementary Materials

This PDF file includes:

Supplementary Methods
Figs. S1 to S8
Legends for tables S1 to S9
References

Other Supplementary Material for this manuscript includes the following:

Tables S1 to S9

REFERENCES AND NOTES

1. H. Sung, J. Ferlay, R. L. Siegel, M. Laversanne, I. Soerjomataram, A. Jemal, F. Bray, Global Cancer Statistics 2020: GLOBOCAN Estimates of Incidence and Mortality Worldwide for 36 Cancers in 185 Countries. *CA Cancer J. Clin.* **71**, 209–249 (2021).
2. C. M. Perou, T. Sørlie, M. B. Eisen, M. van de Rijn, S. S. Jeffrey, C. A. Rees, J. R. Pollack, D. T. Ross, H. Johnsen, L. A. Akslen, O. Fluge, A. Pergamenschikov, C. Williams, S. X. Zhu, P. E. Lønning, A. L. Børresen-Dale, P. O. Brown, D. Botstein, Molecular portraits of human breast tumours. *Nature* **406**, 747–752 (2000).
3. Cancer Genome Atlas Network, Comprehensive molecular portraits of human breast tumours. *Nature* **490**, 61–70 (2012).
4. D. Zardavas, A. Irrthum, C. Swanton, M. Piccart, Clinical management of breast cancer heterogeneity. *Nat. Rev. Clin. Oncol.* **12**, 381–394 (2015).
5. N. C. Turner, J. S. Reis-Filho, Genetic heterogeneity and cancer drug resistance. *Lancet Oncol.* **13**, e178–e185 (2012).
6. S. C. Dentro, I. Leshchiner, K. Haase, M. Tarabichi, J. Wintersinger, A. G. Deshwar, K. Yu, Y. Rubanova, G. Macintyre, J. Demeulemeester, I. Vázquez-García, K. Kleinheinz, D. G. Livitz, S. Malikic, N. Donmez, S. Sengupta, P. Anur, C. Jolly, M. Cmero, D. Rosebrock, S. E. Schumacher, Y. Fan, M. Fittall, R. M. Drews, X. Yao, T. B. K. Watkins, J. Lee, M. Schlesner, H. Zhu, D. J. Adams, N. McGranahan, C. Swanton, G. Getz, P. C. Boutros, M. Imielinski, R. Beroukhim, S. C. Sahinalp, Y. Ji, M. Peifer, I. Martincorena, F. Markowetz, V. Mustonen, K. Yuan, M. Gerstung, P. T. Spellman, W. Wang, Q. D. Morris, D. C. Wedge, P. Van Loo; PCAWG Evolution and Heterogeneity Working Group and the PCAWG Consortium, Characterizing genetic intra-tumor heterogeneity across 2,658 human cancer genomes. *Cell* **184**, 2239–2254.e39 (2021).
7. A. Marusyk, M. Janiszewska, K. Polyak, Intratumor heterogeneity: The Rosetta stone of therapy resistance. *Cancer Cell* **37**, 471–484 (2020).
8. N. McGranahan, C. Swanton, Clonal heterogeneity and tumor evolution: past, present, and the future. *Cell* **168**, 613–628 (2017).
9. M. Greaves, C. C. Maley, Clonal evolution in cancer. *Nature* **481**, 306–313 (2012).
10. P. C. Nowell, The clonal evolution of tumor cell populations. *Science* **194**, 23–28 (1976).
11. L. R. Yates, M. Gerstung, S. Knappskog, C. Desmedt, G. Gundem, P. Van Loo, T. Aas, L. B. Alexandrov, D. Larsimont, H. Davies, Y. Li, Y. S. Ju, M. Ramakrishna, H. K. Haugland, P. K. Lilleng, S. Nik-Zainal, S. McLaren, A. Butler, S. Martin, D. Glodzik, A. Menzies, K. Raine, J. Hinton, D. Jones, L. J. Mudie, B. Jiang, D. Vincent, A. Greene-Colozzi, P. Y. Adnet, A. Fatima, M. Maetens, M. Ignatiadis, M. R. Stratton, C. Sotiriou, A. L. Richardson, P. E. Lønning, D. C. Wedge, P. J. Campbell, Subclonal diversification of primary breast cancer revealed by multiregion sequencing. *Nat. Med.* **21**, 751–759 (2015).
12. W. T. Barry, D. N. Kernagis, H. K. Dressman, R. J. Griffis, J. D. Hunter, J. A. Olson, J. R. Marks, G. S. Ginsburg, P. K. Marcom, J. R. Nevins, J. Geradts, M. B. Datto, Intratumor heterogeneity and precision of microarray-based predictors of breast cancer biology and clinical outcome. *J. Clin. Oncol.* **28**, 2198–2206 (2010).
13. A. Roth, J. Khattra, D. Yap, A. Wan, E. Laks, J. Biele, G. Ha, S. Aparicio, A. Bouchard-Cote, S. P. Shah, PyClone: Statistical inference of clonal population structure in cancer. *Nat. Methods* **11**, 396–398 (2014).
14. E. A. Mroz, J. W. Rocco, MATH, a novel measure of intratumor genetic heterogeneity, is high in poor-outcome classes of head and neck squamous cell carcinoma. *Oral Oncol.* **49**, 211–215 (2013).
15. R. Xue, R. Li, H. Guo, L. Guo, Z. Su, X. Ni, L. Qi, T. Zhang, Q. Li, Z. Zhang, X. S. Xie, F. Bai, N. Zhang, Variable intra-tumor genomic heterogeneity of multiple lesions in patients with hepatocellular carcinoma. *Gastroenterology* **150**, 998–1008 (2016).
16. N. Andor, T. A. Graham, M. Jansen, L. C. Xia, C. A. Aktipis, C. Petritsch, H. P. Ji, C. C. Maley, Pan-cancer analysis of the extent and consequences of intratumor heterogeneity. *Nat. Med.* **22**, 105–113 (2016).
17. P. Lambin, E. Rios-Velazquez, R. Leijenaar, S. Carvalho, R. G. van Stiphout, P. Granton, C. M. Zegers, R. Gillies, R. Boellard, A. Dekker, H. J. Aerts, Radiomics: Extracting more information from medical images using advanced feature analysis. *Eur. J. Cancer* **48**, 441–446 (2012).
18. J. P. O'Connor, C. J. Rose, J. C. Waterton, R. A. Carano, G. J. Parker, A. Jackson, Imaging intratumor heterogeneity: Role in therapy response, resistance, and clinical outcome. *Clin. Cancer Res.* **21**, 249–257 (2015).
19. Q. Sun, Y. Chen, C. Liang, Y. Zhao, X. Lv, Y. Zou, K. Yan, H. Zheng, D. Liang, Z. C. Li, Biologic pathways underlying prognostic radiomics phenotypes from paired MRI and RNA sequencing in glioblastoma. *Radiology* **301**, 654–663 (2021).
20. M. Fan, P. Xia, R. Clarke, Y. Wang, L. Li, Radiogenomic signatures reveal multiscale intratumour heterogeneity associated with biological functions and survival in breast cancer. *Nat. Commun.* **11**, 4861 (2020).
21. J. J. M. van Griethuysen, A. Fedorov, C. Parmar, A. Hosny, N. Aucoin, V. Narayan, R. G. H. Beets-Tan, J. C. Fillion-Robin, S. Pieper, H. J. W. L. Aerts, Computational radiomics system to decode the radiographic phenotype. *Cancer Res.* **77**, e104–e107 (2017).
22. T. Keenan, B. Moy, E. A. Mroz, K. Ross, A. Niemierko, J. W. Rocco, S. Isakoff, L. W. Ellisen, A. Bardia, Comparison of the genomic landscape between primary breast cancer in african american versus white women and the association of racial differences with tumor recurrence. *J. Clin. Oncol.* **33**, 3621–3627 (2015).
23. N. Just, Improving tumour heterogeneity MRI assessment with histograms. *Br. J. Cancer* **111**, 2205–2213 (2014).
24. R. D. Chitalia, J. Rowland, E. S. McDonald, L. Pantalone, E. A. Cohen, A. Gastounioti, M. Feldman, M. Schnall, E. Conant, D. Kontos, Imaging phenotypes of breast cancer heterogeneity in preoperative breast dynamic contrast enhanced magnetic resonance imaging (DCE-MRI) scans predict 10-year recurrence. *Clin. Cancer Res.* **26**, 862–869 (2020).
25. H. J. Aerts, E. R. Velazquez, R. T. Leijenaar, C. Parmar, P. Grossmann, S. Carvalho, J. Bussink, R. Monshouwer, B. Haibe-Kains, D. Rietveld, F. Hoebers, M. M. Rietbergen, C. R. Leemans, A. Dekker, J. Quackenbush, R. J. Gillies, P. Lambin, Decoding tumour phenotype by noninvasive imaging using a quantitative radiomics approach. *Nat. Commun.* **5**, 4006 (2014).
26. L. Jiang, C. You, Y. Xiao, H. Wang, G. H. Su, B. Q. Xia, R. C. Zheng, D. D. Zhang, Y. Z. Jiang, Y. J. Gu, Z. M. Shao, Radiogenomic analysis reveals tumor heterogeneity of triple-negative breast cancer. *Cell Rep. Med.* **3**, 100694 (2022).
27. J. Wu, G. Cao, X. Sun, J. Lee, D. L. Rubin, S. Napel, A. W. Kurian, B. L. Daniel, R. Li, Intratumoral spatial heterogeneity at perfusion MR imaging predicts recurrence-free survival in locally advanced breast cancer treated with neoadjuvant chemotherapy. *Radiology* **288**, 26–35 (2018).
28. W. L. Bi, A. Hosny, M. B. Schabath, M. L. Giger, N. J. Birkbak, A. Mehrtash, T. Allison, O. Arnaout, C. Abbosh, I. F. Dunn, R. H. Mak, R. M. Tamimi, C. M. Tempany, C. Swanton, U. Hoffmann, L. H. Schwartz, R. J. Gillies, R. Y. Huang, H. Aerts, Artificial intelligence in cancer imaging: Clinical challenges and applications. *CA Cancer J. Clin.* **69**, 127–157 (2019).
29. X. Hua, W. Zhao, A. C. Pesatori, D. Consonni, N. E. Caporaso, T. Zhang, B. Zhu, M. Wang, K. Jones, B. Hicks, L. Song, J. Sampson, D. C. Wedge, J. Shi, M. T. Landi, Genetic and epigenetic intratumor heterogeneity impacts prognosis of lung adenocarcinoma. *Nat. Commun.* **11**, 2459 (2020).
30. M. Greaves, Evolutionary determinants of cancer. *Cancer Discov.* **5**, 806–820 (2015).
31. X. Jiang, B. R. Stockwell, M. Conrad, Ferroptosis: Mechanisms, biology and role in disease. *Nat. Rev. Mol. Cell Biol.* **22**, 266–282 (2021).
32. N. Zhang, G. Shu, E. Qiao, X. Xu, L. Shen, C. Lu, W. Chen, S. Fang, Y. Yang, J. Song, Z. Zhao, J. Tu, M. Xu, M. Chen, Y. Du, J. Ji, DNA-functionalized liposomes in vivo fusion for NIR-II/MRI guided pretargeted ferroptosis therapy of metastatic breast cancer. *ACS Appl. Mater. Interfaces* **14**, 20603–20615 (2022).

33. P. Zhang, Y. Hou, J. Zeng, Y. Li, Z. Wang, R. Zhu, T. Ma, M. Gao, Coordinatively unsaturated Fe(3+) based activatable probes for enhanced MRI and therapy of tumors. *Angew. Chem. Int. Ed. Engl.* **58**, 11088–11096 (2019).
34. B. Yu, B. Choi, W. Li, D. H. Kim, Magnetic field boosted ferroptosis-like cell death and responsive MRI using hybrid vesicles for cancer immunotherapy. *Nat. Commun.* **11**, 3637 (2020).
35. E. Papaevangelou, G. S. Almeida, Y. Jamin, S. P. Robinson, N. M. deSouza, Diffusion-weighted MRI for imaging cell death after cytotoxic or apoptosis-inducing therapy. *Br. J. Cancer* **112**, 1471–1479 (2015).
36. M. Oshi, S. Gandhi, L. Yan, Y. Tokumaru, R. Wu, A. Yamada, R. Matsuyama, I. Endo, K. Takabe, Abundance of reactive oxygen species (ROS) is associated with tumor aggressiveness, immune response, and worse survival in breast cancer. *Breast Cancer Res. Treat.* **194**, 231–241 (2022).
37. G. Lei, L. Zhuang, B. Gan, Targeting ferroptosis as a vulnerability in cancer. *Nat. Rev. Cancer* **22**, 381–396 (2022).
38. C. Liang, X. Zhang, M. Yang, X. Dong, Recent progress in ferroptosis inducers for cancer therapy. *Adv. Mater.* **31**, e1904197 (2019).
39. E. Llabani, R. W. Hicklin, H. Y. Lee, S. E. Motika, L. A. Crawford, E. Weerapana, P. J. Hergenrother, Diverse compounds from pleuromutilin lead to a thioredoxin inhibitor and inducer of ferroptosis. *Nat. Chem.* **11**, 521–532 (2019).
40. J. Wu, C. Li, M. Gensheimer, S. Padda, F. Kato, H. Shirato, Y. Wei, C. B. Schonlieb, S. J. Price, D. Jaffray, J. Heymach, J. W. Neal, B. W. Loo Jr., H. Wakelee, M. Diehn, R. Li, Radiological tumor classification across imaging modality and histology. *Nat. Mach. Intell.* **3**, 787–798 (2021).
41. K. Clark, B. Vendt, K. Smith, J. Freymann, J. Kirby, P. Koppel, S. Moore, S. Phillips, D. Maffitt, M. Pringle, L. Tarbox, F. Prior, The cancer imaging archive (TCIA): Maintaining and operating a public information repository. *J. Digit. Imaging* **26**, 1045–1057 (2013).
42. B. Wang, A. M. Mezlini, F. Demir, M. Fiume, Z. Tu, M. Brudno, B. Haibe-Kains, A. Goldenberg, Similarity network fusion for aggregating data types on a genomic scale. *Nat. Methods* **11**, 333–337 (2014).
43. C. Leys, C. Ley, O. Klein, P. Bernard, L. Licata, Detecting outliers: Do not use standard deviation around the mean, use absolute deviation around the median. *J. Exp. Soc. Psychol.* **49**, 764–766 (2013).
44. A. Saha, M. R. Harowicz, L. J. Grimm, C. E. Kim, S. V. Ghate, R. Walsh, M. A. Mazurowski, A machine learning approach to radiogenomics of breast cancer: a study of 922 subjects and 529 DCE-MRI features. *Br. J. Cancer* **119**, 508–516 (2018).
45. H. Li, Y. Zhu, E. S. Burnside, K. Drukker, K. A. Hoadley, C. Fan, S. D. Conzen, G. J. Whitman, E. J. Sutton, J. M. Net, M. Ganott, E. Huang, E. A. Morris, C. M. Perou, Y. Ji, M. L. Giger, MR imaging radiomics signatures for predicting the risk of breast cancer recurrence as given by research versions of mammaprint, oncotype DX, and PAM50 gene assays. *Radiology* **281**, 382–391 (2016).
46. B. B. Avants, C. L. Epstein, M. Grossman, J. C. Gee, Symmetric diffeomorphic image registration with cross-correlation: evaluating automated labeling of elderly and neurodegenerative brain. *Med. Image Anal.* **12**, 26–41 (2008).
47. J. G. Sled, A. P. Zijdenbos, A. C. Evans, A nonparametric method for automatic correction of intensity nonuniformity in MRI data. *IEEE Trans. Med. Imaging* **17**, 87–97 (1998).
48. C. M. Thompson, I. Mallawaarachchi, D. K. Dwivedi, A. P. Ayyappan, N. K. Shokar, R. Lakshmanaswamy, A. K. Dwivedi, The association of background parenchymal enhancement at breast MRI with breast cancer: A systematic review and meta-analysis. *Radiology* **292**, 552–561 (2019).
49. S. Y. Kim, N. Cho, S. U. Shin, H. B. Lee, W. Han, I. A. Park, B. R. Kwon, S. Y. Kim, S. H. Lee, J. M. Chang, W. K. Moon, Contrast-enhanced MRI after neoadjuvant chemotherapy of breast cancer: lesion-to-background parenchymal signal enhancement ratio for discriminating pathological complete response from minimal residual tumour. *Eur. Radiol.* **28**, 2986–2995 (2018).
50. S. Wu, W. A. Berg, M. L. Zuley, B. F. Kurland, R. C. Jankowitz, R. Nishikawa, D. Gur, J. H. Sumkin, Breast MRI contrast enhancement kinetics of normal parenchyma correlate with presence of breast cancer. *Breast Cancer Res.* **18**, 76 (2016).
51. C. L. Mercado, BI-RADS update. *Radiol. Clin. North Am.* **52**, 481–487 (2014).
52. A. Fedorov, R. Beichel, J. Kalpathy-Cramer, J. Finet, J. C. Fillion-Robin, S. Pujol, C. Bauer, D. Jennings, F. Fennessy, M. Sonka, J. Buatti, S. Aylward, J. V. Miller, S. Pieper, R. Kikinis, 3D slicer as an image computing platform for the quantitative imaging network. *Magn. Reson. Imaging* **30**, 1323–1341 (2012).
53. Z. Liu, Z. Li, J. Qu, R. Zhang, X. Zhou, L. Li, K. Sun, Z. Tang, H. Jiang, H. Li, Q. Xiong, Y. Ding, X. Zhao, K. Wang, Z. Liu, J. Tian, Radiomics of multiparametric MRI for pretreatment prediction of pathologic complete response to neoadjuvant chemotherapy in breast cancer: A multicenter study. *Clin. Cancer Res.* **25**, 3538–3547 (2019).
54. J. Gamper, N. Alemi Koohbanani, K. Benet, A. Khuram, N. Rajpoot, in *Digital Pathology: 15th European Congress, ECDP 2019, Warwick, UK, April 10–13, 2019, Proceedings 15* (Springer, 2019), pp. 11–19.
55. S. Graham, Q. D. Vu, S. E. A. Raza, A. Azam, Y. W. Tsang, J. T. Kwak, N. Rajpoot, Hover-Net: Simultaneous segmentation and classification of nuclei in multi-tissue histology images. *Med. Image Anal.* **58**, 101563 (2019).
56. H. Mi, T. J. Bivalacqua, M. Kates, R. Seiler, P. C. Black, A. S. Popel, A. S. Baras, Predictive models of response to neoadjuvant chemotherapy in muscle-invasive bladder cancer using nuclear morphology and tissue architecture. *Cell Rep. Med.* **2**, 100382 (2021).
57. D. Freed, R. Aldana, J. A. Weber, J. S. Edwards, The Sentieon Genomics Tools-A fast and accurate solution to variant calling from next-generation sequence data. bioRxiv 10.1101/115717 [Preprint]. 12 May 2017. https://doi.org/10.1101/115717.
58. S. Lee, S. Lee, S. Ouellette, W.-Y. Park, E. A. Lee, P. J. Park, NGSCheckMate: Software for validating sample identity in next-generation sequencing studies within and across data types. *Nucleic Acids Res.* **45**, e103–e103 (2017).
59. S. W. Wingett, S. Andrews, FastQ Screen: A tool for multi-genome mapping and quality control. *F1000Res* **7**, 1338 (2018).
60. S. Andrews, FASTQC: A Quality Control Tool for High Throughput Sequence Data (2014); www.bioinformatics.babraham.ac.uk/projects/.
61. K. Okonechnikov, A. Conesa, F. García-Alcalde, Qualimap 2: advanced multi-sample quality control for high-throughput sequencing data. *Bioinformatics* **32**, 292–294 (2016).
62. D. C. Koboldt, Q. Zhang, D. E. Larson, D. Shen, M. D. McLellan, L. Lin, C. A. Miller, E. R. Mardis, L. Ding, R. K. Wilson, VarScan 2: somatic mutation and copy number alteration discovery in cancer by exome sequencing. *Genome Res.* **22**, 568–576 (2012).
63. D. Freed, R. Pan, R. Aldana, TNscope: accurate detection of somatic mutations with haplotype-based variant candidate detection and machine learning filtering. bioRxiv 10.1101/250647 [Preprint]. 19 January 2018. https://doi.org/10.1101/250647.
64. K. Karczewski, L. Francioli, The genome aggregation database (gnomAD). MacArthur Lab (2017).
65. D. Chakravarty, J. Gao, S. M. Phillips, R. Kundra, H. Zhang, J. Wang, J. E. Rudolph, R. Yaeger, T. Soumerai, M. H. Nissan, M. T. Chang, S. Chandarlapaty, T. A. Traina, P. K. Paik, A. L. Ho, F. M. Hantash, A. Grupe, S. S. Baxi, M. K. Callahan, A. Snyder, P. Chi, D. Danila, M. Gounder, J. J. Harding, M. D. Hellmann, G. Iyer, Y. Janjigian, T. Kaley, D. A. Levine, M. Lowery, A. Omuro, M. A. Postow, D. Rathkopf, A. N. Shoushtari, N. Shukla, M. Voss, E. Paraiso, A. Zehir, M. F. Berger, B. S. Taylor, L. B. Saltz, G. J. Riely, M. Ladanyi, D. M. Hyman, J. Baselga, P. Sabbatini, D. B. Solit, N. Schultz, OncoKB: A precision oncology knowledge base. *JCO Precis. Oncol.* **2017**, PO.17.00011 (2017).
66. M. H. Bailey, C. Tokheim, E. Porta-Pardo, S. Sengupta, D. Bertrand, A. Weerasinghe, A. Colaprico, M. C. Wendl, J. Kim, B. Reardon, P. K.-S. Ng, K. J. Jeong, S. Cao, Z. Wang, J. Gao, Q. Gao, F. Wang, E. M. Liu, L. Mularoni, C. Rubio-Perez, N. Nagarajan, I. Cortes-Ciriano, D. C. Zhou, W. W. Liang, J. M. Hess, V. D. Yellapantula, D. Tamborero, A. Gonzalez-Perez, C. Suphavilai, J. Y. Ko, E. Khurana, P. J. Park, E. M. Van Allen, H. Liang; MC3 Working Group; Cancer Genome Atlas Research Network, M. S. Lawrence, A. Godzik, N. Lopez-Bigas, J. Stuart, D. Wheeler, G. Getz, K. Chen, A. J. Lazar, G. B. Mills, R. Karchin, L. Ding, Comprehensive characterization of cancer driver genes and mutations. *Cell* **174**, 1034–1035 (2018).
67. F. Martinez-Jimenez, F. Muinos, I. Sentis, J. Deu-Pons, I. Reyes-Salazar, C. Arnedo-Pac, L. Mularoni, O. Pich, J. Bonet, H. Kranas, A. Gonzalez-Perez, N. Lopez-Bigas, A compendium of mutational cancer driver genes. *Nat. Rev. Cancer* **20**, 555–572 (2020).
68. P. A. Futreal, L. Coin, M. Marshall, T. Down, T. Hubbard, R. Wooster, N. Rahman, M. R. Stratton, A census of human cancer genes. *Nat. Rev. Cancer* **4**, 177–183 (2004).
69. P. Van Loo, S. H. Nordgard, O. C. Lingjaerde, H. G. Russnes, I. H. Rye, W. Sun, V. J. Weigman, P. Marynen, A. Zetterberg, B. Naume, C. M. Perou, A. L. Borresen-Dale, V. N. Kristensen, Allele-specific copy number analysis of tumors. *Proc. Natl. Acad. Sci. U.S.A.* **107**, 16910–16915 (2010).
70. C. H. Mermel, S. E. Schumacher, B. Hill, M. L. Meyerson, R. Beroukhim, G. Getz, GISTIC2.0 facilitates sensitive and confident localization of the targets of focal somatic copy-number alteration in human cancers. *Genome Biol.* **12**, R41 (2011).
71. Y. Xiao, D. Ma, Y. S. Yang, F. Yang, J. H. Ding, Y. Gong, L. Jiang, L. P. Ge, S. Y. Wu, Q. Yu, Q. Zhang, F. Bertucci, Q. Sun, X. Hu, D. Q. Li, Z. M. Shao, Y. Z. Jiang, Comprehensive metabolomics expands precision medicine for triple-negative breast cancer. *Cell Res.* **32**, 477–490 (2022).
72. F. Nassiri, J. Liu, V. Patil, Y. Mamatjan, J. Z. Wang, R. Hugh-White, A. M. Macklin, S. Khan, O. Singh, S. Karimi, R. I. Corona, L. Y. Liu, C. Y. Chen, A. Chakravarthy, Q. Wei, B. Mehani, S. Suppiah, A. Gao, A. M. Workewych, G. Tabatabai, P. C. Boutros, G. D. Bader, D. D. de Carvalho, T. Kislinger, K. Aldape, G. Zadeh, A clinically applicable integrative molecular classification of meningiomas. *Nature* **597**, 119–125 (2021).
73. A. Subramanian, P. Tamayo, V. K. Mootha, S. Mukherjee, B. L. Ebert, M. A. Gillette, A. Paulovich, S. L. Pomeroy, T. R. Golub, E. S. Lander, J. P. Mesirov, Gene set enrichment

analysis: A knowledge-based approach for interpreting genome-wide expression profiles. *Proc. Natl. Acad. Sci. U.S.A.* **102**, 15545–15550 (2005).

74. S. Hanzelmann, R. Castelo, J. Guinney, GSVA: Gene set variation analysis for microarray and RNA-seq data. *BMC Bioinformatics* **14**, 7 (2013).
75. Y. Xiao, D. Ma, S. Zhao, C. Suo, J. Shi, M. Z. Xue, M. Ruan, H. Wang, J. Zhao, Q. Li, P. Wang, L. Shi, W. T. Yang, W. Huang, X. Hu, K.-D. Yu, S. Huang, F. Bertucci, Y.-Z. Jiang, Z.-M. Shao; AME Breast Cancer Collaborative Group, Multi-omics profiling reveals distinct microenvironment characterization and suggests immune escape mechanisms of triple-negative breast cancer. *Clin. Cancer Res.* **25**, 5002–5014 (2019).
76. R. Possemato, K. M. Marks, Y. D. Shaul, M. E. Pacold, D. Kim, K. Birsoy, S. Sethumadhavan, H. K. Woo, H. G. Jang, A. K. Jha, W. W. Chen, F. G. Barrett, N. Stransky, Z. Y. Tsun, G. S. Cowley, J. Barretina, N. Y. Kalaany, P. P. Hsu, K. Ottina, A. M. Chan, B. Yuan, L. A. Garraway, D. E. Root, M. Mino-Kenudson, E. F. Brachtel, E. M. Driggers, D. M. Sabatini, Functional genomics reveal that the serine synthesis pathway is essential in breast cancer. *Nature* **476**, 346–350 (2011).
77. B. J. Crielaard, T. Lammers, S. Rivella, Targeting iron metabolism in drug discovery and delivery. *Nat. Rev. Drug Discov.* **16**, 400–423 (2017).
78. A. A. Hakimi, E. Reznik, C. H. Lee, C. J. Creighton, A. R. Brannon, A. Luna, B. A. Aksoy, E. M. Liu, R. Shen, W. Lee, Y. Chen, S. M. Stirdivant, P. Russo, Y. B. Chen, S. K. Tickoo, V. E. Reuter, E. H. Cheng, C. Sander, J. J. Hsieh, An integrated metabolic atlas of clear cell renal cell carcinoma. *Cancer Cell* **29**, 104–116 (2016).

Acknowledgments: We appreciate TCIA for curating the original DCE-MRI for free download and analysis. **Funding:** This work was supported by grants from the National Natural Science Foundation of China (92159301, 82272822, 81901703, 82071878, 82002792, 82271957, and 91959207), the Shanghai Rising-Star Program (20YF1408600), the Shanghai Key Laboratory of Breast Cancer (12DZ2260100), the Clinical Research Plan of SHDC (SHDC2020CR2008A and SHDC12021103), the SHDC Municipal Project for Developing Emerging and Frontier Technology in Shanghai Hospitals (SHDC12021103), Shanghai Medical Innovation Research Project (22Y11912700), Shanghai Natural Science Foundation (20ZR1406400), and Shanghai Municipal Science and Technology Major Project (2018SHZDZX01). The funders had no role in the study design, data collection and analysis, decision to publish, or preparation of the manuscript. **Author contributions:** Conceptualization: Y.-Z.J., Z.-M.S., and Y.X. Methodology: G.-H.S., C.Y., R.-C.Z., and S.Z. Data curation: C.Y., R.-C.Z., S.-Y.S., J.-Y.Z., and L.-Y.L. Investigation: G.-H.S. and Y.X. Formal analysis: G.-H.S. Writing—original draft: G.-H.S., C.Y., R.-C.Z., and S.Z. Writing—review and editing: Y.X. and Y.-Z.J. Supervision: Z.-M.S., Y.-J.G., Y.-Z.J., and H.W. All authors approved the final manuscript. **Competing interests:** The authors declare that they have no competing interests. **Data and materials availability:** Original images of DUKE and TCGA breast MRI are publicly available at https://doi.org/10.7937/TCIA.e3sv-re93 and https://doi.org/10.7937/K9/TCIA.2016.AB2NAZRP. Radiomics data from FUSCC cohort have been deposited in Zenodo (https://doi.org/10.5281/zenodo.8273240). Matched multiomics data can be viewed in The National Omics Data Encyclopedia (NODE) (www.biosino.org/node) by pasting the accession (OEP003049) into the text search box or through the URL: www.biosino.org/node/project/detail/OEP003049. All data needed to evaluate the conclusions in the paper are present in the paper and/or the Supplementary Materials.

Submitted 28 September 2022
Accepted 6 September 2023
Published 6 October 2023
10.1126/sciadv.adf0837